

# An extreme case of galaxy and cluster co-evolution at $z = 0.7$

H. Ebeling<sup>1</sup>★, J. Richard<sup>2</sup>, I. Smail<sup>3</sup>, A. C. Edge<sup>3</sup>, A. M. Koekemoer<sup>4</sup>, L. Zalesky<sup>1</sup>

<sup>1</sup> *Institute for Astronomy University of Hawaii, 2680 Woodlawn Drive Honolulu, HI 96822, USA*

<sup>2</sup> *Univ Lyon, Univ Lyon1, Ens de Lyon, CNRS, Centre de Recherche Astrophysique de Lyon UMR5574, F-69230, Saint-Genis-Laval, France*

<sup>3</sup> *Centre for Extragalactic Astronomy, Department of Physics, Durham University, South Road, Durham DH1 3LE, UK*

<sup>4</sup> *Space Telescope Science Institute, 3700 San Martin Dr., Baltimore, MD 21218, USA*

Accepted 2021 September 16. Received 2021 September 2; in original form 2020 December 2

## ABSTRACT

We report the discovery of eMACS J0252.4–2100 (eMACS J0252), a massive and highly evolved galaxy cluster at  $z = 0.703$ . Our analysis of *Hubble Space Telescope* imaging and VLT/MUSE and Keck/DEIMOS spectroscopy of the system finds a high velocity dispersion of  $1020^{+180}_{-190}$  km s<sup>−1</sup> and a high (if tentative) X-ray luminosity of  $(1.2 \pm 0.4) \times 10^{45}$  erg s<sup>−1</sup> (0.1–2.4 keV). As extreme is the system’s brightest cluster galaxy, a giant cD galaxy that forms stars at a rate of between 85 and 300 M<sub>⊙</sub> yr<sup>−1</sup> and features an extended halo of diffuse [O II] emission, as well as evidence of dust. Its most remarkable properties, however, are an exceptionally high ellipticity and a radially symmetric flow of gas in the surrounding intracluster medium, potential direct kinematic evidence of a cooling flow. A strong-lensing analysis, anchored by two multiple-image systems with spectroscopic redshifts, finds the best lens model to consist of a single cluster-scale halo with a total mass of  $(1.9 \pm 0.1) \times 10^{14}$  M<sub>⊙</sub> within 250 kpc of the cluster core and, again, an extraordinarily high ellipticity of  $e = 0.8$ . Although further, in-depth studies across the electromagnetic spectrum (especially in the X-ray regime) are needed to conclusively determine the dynamical state of the system, the properties established so far suggest that eMACS J0252 must have already been highly evolved well before  $z \sim 1$ , making it a prime target to constrain the physical mechanisms and history of the co-evolution of dark-matter halos and baryons in the era of cluster formation.

**Key words:** gravitational lensing: strong – galaxies: clusters: general

## 1 INTRODUCTION

In the widely accepted paradigm of hierarchical structure formation, galaxy clusters form through successive mergers. As a result, the fraction of undisturbed (“relaxed”) clusters decreases monotonically with increasing redshift in a trend that becomes profound at  $z > 0.4$  (Mann & Ebeling 2012) but may weaken again at yet higher redshifts (Nurgaliev et al. 2017). In parallel, the giant elliptical galaxies at the hearts of clusters grow through similar merger and accretion processes, resulting in brightest cluster galaxies (BCGs) that represent the by far most massive concentrations of stars in the Universe. It has long been known that the evolution of BCGs and their host clusters are closely linked (e.g., Dressler 1984; Kormendy & Djorgovski 1989; Lin & Mohr 2004; De Lucia & Blaizot 2007; Coziol et al. 2009; Lauer et al. 2014); however, to which extent the rate of BCG evolution tracks that of the host cluster remains a subject of debate (Bellstedt et al. 2016, and references therein).

cD galaxies constitute a special class of BCG: found almost exclusively in fully relaxed clusters, they are characterized most readily by their enormous sizes, extreme luminosities, and (in rich clusters) extended, low-surface-brightness halos (Matthews et al. 1964; Oemler 1976; Schombert 1986; Newman et al. 2013; Wen & Han 2013). Not only are such extreme galaxies absent from the low-density field;

even within the already overdense environment of galaxy clusters they invariably mark the center of pronounced mass overdensities (e.g., Beers & Geller 1983). In recognition of the unique position of cD galaxies at the extreme end of the galaxy mass and luminosity functions, BCG evolution and its interconnection with the cluster environment remains an area of intense study. Of particular interest are the questions of whether BCG growth occurs mostly early on (suggested by numerical simulations and supported by the fact that cD galaxies can form already in high-density galaxy groups; Albert et al. 1977; Thuan & Romanishin 1981; Merritt 1984); at intermediate times in the process of cluster mergers (consistent with the high frequency of cDs with multiple nuclei; Schneider et al. 1983; Tonry 1985; Kluge et al. 2020); or late, during cluster virialization (supported, e.g., by the prevalence of dust and star formation in cD galaxies in cool-core clusters, or the strong link between the luminous envelopes of cD galaxies and the distribution of intra-cluster light; McNamara & O’Connell 1989; O’Dea et al. 2008; Kluge et al. 2020).

If we are to understand which physical mechanisms dominate the co-evolution of clusters and BCGs, we need to identify and study extreme cases across the widest accessible range of redshifts. The most striking example of a fully relaxed cluster hosting a BCG with enhanced star formation and nuclear activity is the Phoenix Cluster at  $z = 0.6$  (McDonald et al. 2012, 2014). At even higher redshifts, recent studies of distant optically and infra-red selected clusters have found

★ E-mail: ebeling@ifa.hawaii.edu

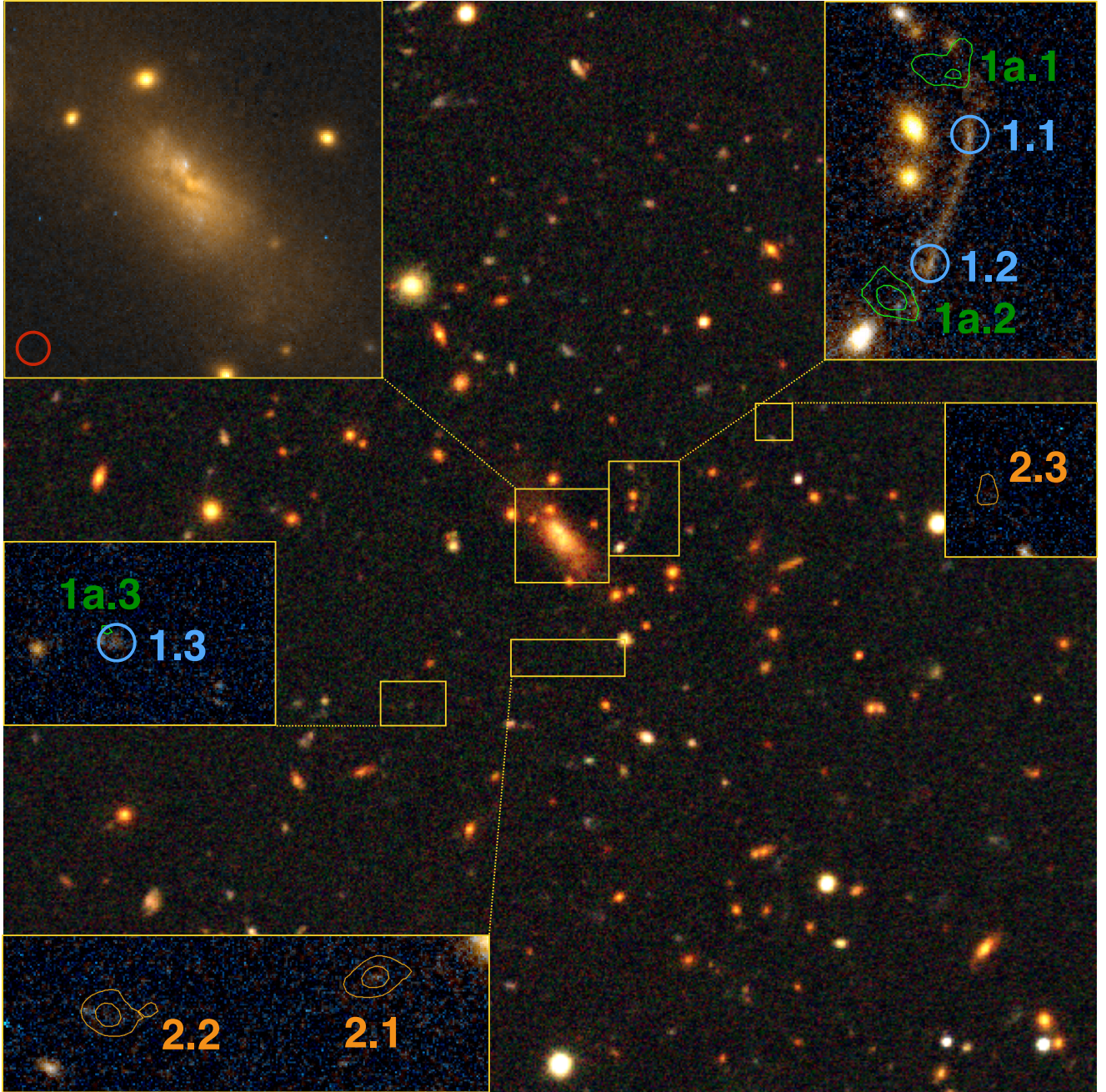


**Figure 1.** Groundbased image ( $g, r, i$ ) of eMACS J0252 as obtained with Gemini-N/GMOS, covering 1 Mpc on the side at the cluster redshift. The insets show the BCG as well as (at increased contrast) strong-lensing features as seen with *HST*/WFC3 (F200LP+F110W; GO-15703) and MUSE ( $\text{Ly}\alpha$  contours, see Section 3.1.3 for details). For illustrative purposes, the red circle shows the approximate size of the seeing disk of our groundbased observations. Note the very extended stellar distribution in the BCG and signs of both a dust lane and dual nuclei.

evidence for enhanced star formation and AGN activity in BCGs at  $z > 1$  (Bonaventura et al. 2017; Trudeau et al. 2019). However, these clusters are not only significantly less massive than the majority of distant clusters selected by X-ray and SZ techniques, they are also not dynamically relaxed and do not host giant central galaxies like the Phoenix Cluster or, at lower redshift, A 1835 ( $z = 0.252$ ; McNamara et al. 2006).

Recent observations of eMACS J0252.4–2100 ( $z = 0.703$ ), the subject of this paper, offer an opportunity to obtain evidence of the interplay of BCG and cluster evolution in a redshift-mass regime

poorly sampled by earlier work. Our paper is structured as follows: we provide an overview of all observations used in our analysis in Section 2, and discuss physical properties of the BCG and the host cluster in Section 3, before presenting our conclusions and plans for further study in Section 4.

We assume the  $\Lambda$ CDM concordance cosmology with  $\Omega_m = 0.3$ ,  $\Omega_\Lambda = 0.7$ , and  $H_0 = 100h \text{ km s}^{-1} \text{ Mpc}^{-1}$ , with  $h = 0.7$ .



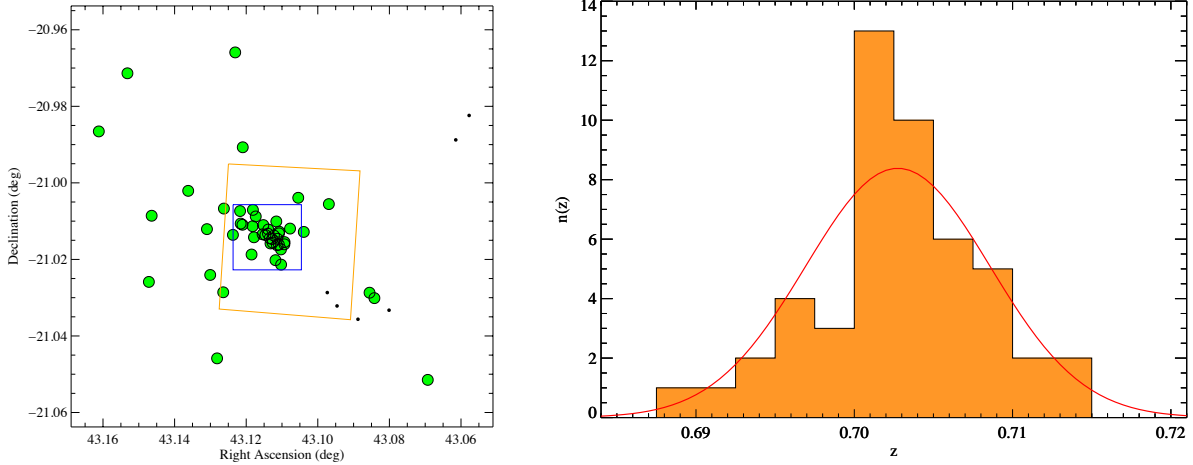


**Figure 2.** *Left:* Spatial distribution of galaxies with spectroscopic redshifts in the range from  $z=0.65$  to  $0.75$  from our DEIMOS and MUSE observations. Cluster members (redshifts within three times the cluster velocity dispersion) are highlighted as filled green circles; the blue and orange rectangles delineate the field of view of MUSE and WFC3/NIR, respectively. Note the alignment of the distribution of cluster members with the major axis of the BCG from Figure 1. *Right:* Histogram of the redshifts of spectroscopic galaxy members for eMACS J0252, as derived from the observations described in Section 2.3. The velocity dispersion of the overlaid, best-fit Gaussian is  $1020^{+180}_{-190}$  km s $^{-1}$ . We find no strong evidence of substructure along the line of sight.

## 2 OBSERVATIONS AND DATA REDUCTION

### 2.1 eMACS J0252.4–2100

The galaxy cluster eMACS J0252.4–2100 ( $z = 0.703$ , hereafter eMACS J0252) was discovered by the eMACS project (Ebeling et al. 2013) in November 2014, when spectroscopic follow-up observations of an overdensity of galaxies around the X-ray source 1RXS J025227.2–210031, detected in the *ROSAT* All-Sky Survey (RASS; Voges et al. 1999), established an approximate redshift of  $z = 0.698$  for the associated galaxy cluster. While the Sunyaev-Zel’dovich (SZ) signal of the system was missed by the *Planck* mission (no corresponding entry is listed in the sample published in Planck Collaboration et al. 2016), the cluster was – according to Gladders et al. (2019) – detected in SZ observations conducted with the South Pole Telescope (SPT) and is listed as SPT-CLJ0252–2100 in the online supplement to Bleem et al. (2020).

### 2.2 Optical and Near-infrared Imaging

We observed eMACS J0252 with the GMOS camera on the Gemini-North 8.1-m telescope atop Maunakea on September 9, 2015 (Program ID GN–2015B–Q-42, PI Ebeling). Three dithered exposures of 90s duration each were taken in each of the  $g'$ ,  $r'$ , and  $i'$  passbands. We used standard data reduction procedures as provided by the Gemini data analysis pipeline to create bias-subtracted, flat-fielded, and fringe-corrected co-added images for each filter. A color image of a 1 Mpc square region around the cluster, based on our GMOS data, is shown in Fig. 1.

On Dec. 13, 2018, eMACS J0252 was observed with the Wide Field Camera 3 (WFC3) aboard the *Hubble Space Telescope* (HST) for the SNAPshot program GO-15307 (PI Gladders). WFC3 obtained images in the F200LP and the F110W filters, using the camera’s UVIS and IR channels, respectively. The former filter covers the UV and optical regime from approximately 2000Å to 8000Å, whereas the latter extends from 9000Å to 1.4  $\mu$ m at near-infrared wavelengths. Three dithered exposures were obtained in each filter, with total exposure times of 741s and 758s for the F200LP and

F110W images, respectively. After initial default calibration by the *HST* archive pipeline, these images were subsequently processed through additional calibration and alignment routines, following approaches described in more detail in Koekemoer et al. (2011). In particular, these subsequent steps resulted in improved astrometric alignment between all the exposures, across both filters, to an accuracy of a few milliarcseconds (rms), as well as improved cleaning of cosmic rays and other detector defects compared to the original archival products. The final combined mosaics for both filters are drizzled to a scale of 30 milliarcseconds per pixel.

Images of salient features within the cluster core, created from the *HST* data, are shown as insets in Fig. 1.

### 2.3 Spectroscopy

After the initial identification of eMACS J0252 as an X-ray luminous galaxy cluster through redshift measurements with the DEIMOS spectrograph (Faber et al. 2003) on the Keck-II 10m telescope on Maunakea (see Sec. 2.1), additional spectroscopic observations of presumed cluster member galaxies were performed with the same telescope and instrument in December 2018, using again the 600 line mm $^{-1}$  grating and the GG455 blocking filter. Applying standard data reduction techniques, we extracted two- and one-dimensional spectra and determined redshifts from cross correlations with template spectra using an adapted version of the software package developed by Masters & Capak (2011).

eMACS J0252 was subsequently observed with the MUSE Integral-Field Unit on the 8.2-m UT4 telescope of the European Southern Observatory’s Very Large Telescope on Cerro Paranal (Chile) on Sep. 6, 2019. Three dithered 970s integrations were obtained in 0.95'' seeing for program 0103.A-0777(A) (PI Edge) in WFM-NOAO-N mode. The MUSE data were reduced using v2.7 of the MUSE data reduction pipeline (Weilbacher et al. 2020), following standard reduction recipes for instrumental calibration and sky subtraction, including specific improvements for self-calibration and masking of interstacks as described in detail in Richard et al. (2020). The field of view of the final combined datacube covers  $1 \times 1$

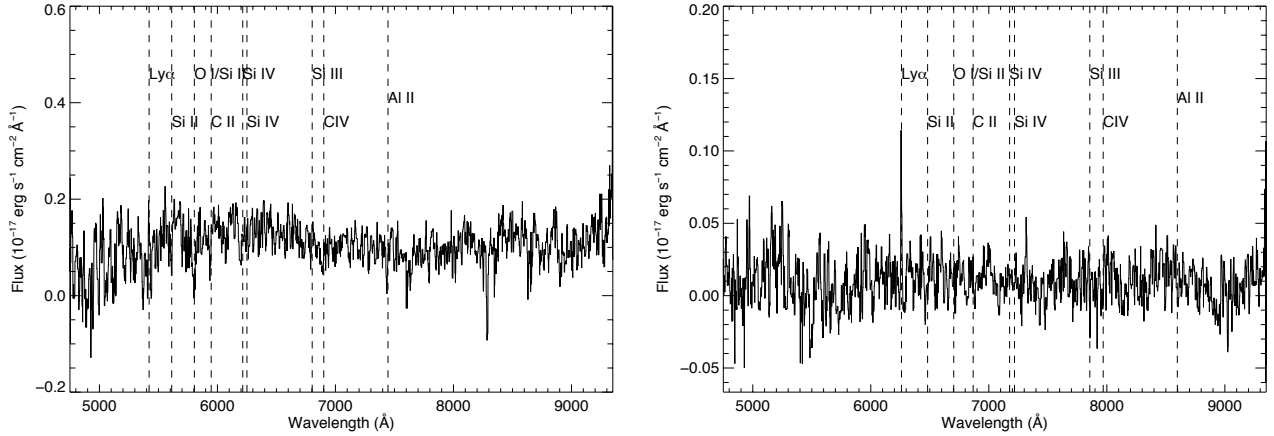


**Figure 3.** MUSE spectra of the two multiple-image systems identified by us in eMACS J0252. *Left:* both components of System 1 ( $z = 3.458$ ); *right:* Image 1 of System 2 ( $z = 4.148$ ).

arcmin<sup>2</sup> centered on the cluster BCG, sampled at a 0.2'' pixel scale. The wavelength range covers 4750–9350 Å at 1.25 Å per pixel, with a spectral resolution  $R \sim 2700$ . We extracted spectra from continuum sources using the *HST*/F110W image as an input catalog. We also searched for line emitters in the reduced datacube using the *muse1et* software, which is part of the MPDAF python package (Piqueras et al. 2019).

The distribution on the equatorial sky of galaxies with spectroscopic redshifts in the range from  $z = 0.65$  to  $0.75$  obtained from our observations is shown in Fig. 2.

### 2.3.1 Radio and Submillimetre

A search of public radio surveys (TGSS, GLEAM, WISH, NVSS, and VLASS) at the location of the BCG of eMACS J0252 reveals a relatively bright, compact radio source detected from 76 MHz to 3 GHz.

A short SCUBA2 observation of eMACS J0252 was obtained at 850  $\mu$ m in August 2015 as part of a larger survey of eMACS clusters (PI Edge). The exposure of 50 min in good conditions ( $\tau_{225} = 0.06$ ) achieved an rms sensitivity of 4.2 mJy per beam; the lack of a detection in this observation places  $3\text{-}\sigma$  upper limits of 12.6 mJy on the BCG flux density at 850  $\mu$ m.

## 3 ANALYSIS AND RESULTS

As is evident from Fig. 1, the optical appearance of eMACS J0252 is heavily dominated by the system's highly elliptical BCG. We here examine key physical properties of both the exceptional galaxy at the core of eMACS J0252 and of its cluster environment.

### 3.1 Cluster properties

#### 3.1.1 Radial velocities

The spectroscopic observations described in Section 2.3 yield a heliocentric cluster redshift of  $z = 0.7028$  and a velocity dispersion of  $\sigma = 1020^{+180}_{-190}$  km s<sup>-1</sup>, based on the 49 concordant redshifts shown in Fig. 2 and listed in the Appendix.

We find no significant substructure along the line of sight in the

overall redshift distribution (Fig. 2), as would be expected if the observed velocity dispersion were inflated by ongoing or recent merger activity perpendicular to the plane of the sky.

The large clustercentric distances reached in our DEIMOS observations enable us to probe the large-scale environment of eMACS J0252 (Fig. 2) and test whether the system is isolated in three dimensions or connected to mass concentrations in the vicinity. However, the redshift distribution of the galaxies observed to date exhibits no clear trends with either right ascension or declination.

#### 3.1.2 X-ray properties

At the cluster redshift of  $z = 0.703$ , the X-ray flux detected in the RASS corresponds to an X-ray luminosity of  $(1.2 \pm 0.4) \times 10^{45}$  erg s<sup>-1</sup> (0.1–2.4 keV). Although, at face value, this measurement suggests that eMACS J0252 is one of a mere handful of exceptionally X-ray luminous clusters known at  $z > 0.6$ , this assessment remains subject to significant uncertainty, owing to the RASS detection in the direction of the source consisting of a mere 12 net photons. A robust determination of the X-ray properties of eMACS J0252 will have to account for contamination from X-ray point sources, a task that requires much better angular resolution than is achieved in past or current X-ray all-sky surveys (*ROSAT* and *eROSITA*).

#### 3.1.3 Strong gravitational lensing

Scrutiny of the spectra obtained with MUSE (Section 2.3) reveals unambiguous signs of strong gravitational lensing in the form of two multiple-image systems. The giant arc almost due West of the BCG is found to consist of two merged images of a galaxy at  $z = 3.458$ . We show the MUSE spectrum of the arc in Fig. 3 (left); features anchoring the redshift measurement are faint Ly $\alpha$  emission spatially offset from the continuum (and included as subsystem 1a in our modeling of the mass distribution), as well as Si II and C II absorption. A second multiple-image system is spectroscopically identified through pronounced Ly $\alpha$  emission at 5420 Å, revealing the source redshift to be  $z = 4.148$  (Fig. 3, right). The components of all multiple-image systems are listed in Table 1 and shown and labeled in the insets to Fig. 1; for Systems 1a and 2, which are barely detected in the *HST* SNAPSHOT of eMACS J0252, we mark the image positions by overlaying contours of the Ly $\alpha$  flux from our MUSE observations.



Image ID	R.A. (J2000)	Dec. (J2000)	$z_{\text{spec}}$
1.1	02 52 26.46	-21 00 46.3	3.458
1.2	02 52 26.55	-21 00 50.4	
1.3	02 52 28.61	-21 01 12.8	
1a.1	02 52 26.51	-21 00 44.2	
1a.2	02 52 26.63	-21 00 51.4	
1a.3	02 52 28.62	-21 01 12.4	4.148
2.1	02 52 26.93	-21 01 05.7	
2.2	02 52 27.51	-21 01 06.9	
2.3	02 52 25.41	-21 00 36.6	

**Table 1.** Multiple-image families identified in the strong-lensing regime of eMACS J0252; see also Figs. 1 (insets) and 3.

We use LENSTOOL (Jullo et al. 2007) to create a lens model of eMACS J0252. Adopting double Pseudo Isothermal Elliptical (dPIE) profiles for the mass distributions of both cluster- and galaxy-scale components, we optimise the shape and mass scaling parameters of the cluster-scale component and the central BCG to reproduce the three multiple-image systems. We include all spectroscopically confirmed cluster members as galaxy-scale halos that act as local perturbers of the large-scale gravitational potential. The best-fit model, characterized by the parameters listed in Table 2, yields an rms offset of  $0.09''$  between the predicted and observed locations of all images. Like the distribution of optical light from the BCG, the mass distribution of eMACS J0252 is characterized by an exceptionally high ellipticity; our lens model requires an axis ratio of  $b/a = 0.34 \pm 0.01$  or an ellipticity of  $e = 0.79$ ,<sup>1</sup> a value far more extreme of the average of 0.52 found, e.g., from statistical gravitational-lensing analyses of SDSS clusters (Shin et al. 2018).

The critical lines (for a source at  $z = 3.458$ ) from the best-fitting lens model are shown in Fig. 4. The projected mass within a radius of 250 kpc is  $(1.94 \pm 0.02 \pm 0.1) \times 10^{14} M_{\odot}$  (statistical and estimated systematic uncertainties are listed separately); the total mass (not well constrained by strong-lensing measurements) exceeds  $5 \times 10^{14} M_{\odot}$ . With an effective Einstein radius<sup>2</sup> of  $19.9''$  for System 1 at  $z = 3.458$  ( $15.5''$  for a source at  $z = 2$ ), eMACS J0252 is a moderately strong gravitational lens, in agreement with the general trend for more powerful cluster lenses to be disturbed active mergers, extreme cases being MACSJ0717.5+3745 (e.g., Limousin et al. 2016) or Abell 2744 (e.g., Jauzac et al. 2015).

## 3.2 BCG properties

### 3.2.1 Optical photometry and morphology

The cD galaxy ( $\alpha_{J2000} = 02^{\text{h}} 52^{\text{m}} 27.25^{\text{s}}$ ,  $\delta_{J2000} = -21^{\circ} 00' 51.2''$ ; Figure 1) in the core of eMACS J0252 is characterized by a prodigious luminosity ( $M_g = -24.1$ ), intersecting dust lanes, and an overall morphology that shows a strong resemblance to BCGs in cool-core clusters at lower redshift (Donahue et al. 2015). The archival photometry from PanSTARRS-1, GALEX and WISE yields a luminosity of  $5 \times 10^{11} L_{\odot}$  for the BCG in the rest-frame  $i$ -band and near-UV, optically blue colours similar to those of line-emitting BCGs at lower redshift (Green et al. 2016).

<sup>1</sup> We define ellipticity as  $e = \frac{1-(b/a)^2}{1+(b/a)^2}$ , with  $b/a$  being the axis ratio.

<sup>2</sup> We define the effective Einstein radius as  $\sqrt{A_{\text{crit}}/\pi}$ , where  $A_{\text{crit}}$  is the area enclosed by the critical line.

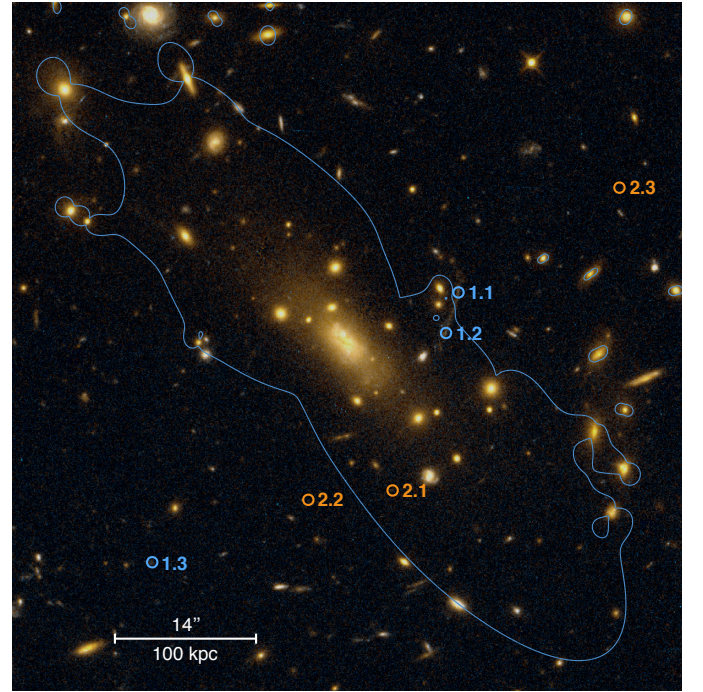


**Figure 4.** Critical line (for a source at  $z = 3.458$ ) of the lens model derived from the strong-lensing constraints listed in Table 1, overlaid on the *HST* image of eMACS J0252. For clarity we do not show the (very similar) critical line for the source redshift of multiple-image system 2.

Even more remarkable is the BCG's extreme elongation (see Figure 1 and 4). Its ellipticity of  $e = 0.78$  (derived from an axis ratio of 0.35 measured from *HST* imaging) is unrivaled among similarly massive clusters (Herbonnet et al. 2019) and a  $> 3\sigma$  outlier compared to the average axis ratio of  $0.7 \pm 0.1$  established for BCGs in general (Donzelli et al. 2011). Although the light envelopes of BCGs are known to become more elliptical with increasing radius, axis ratios below 0.4 are extremely rare and only observed at radii of at least 100 kpc (Kluge et al. 2020), far larger than the approximately 40 kpc probed by our shallow *HST* data (Fig. 6).

### 3.2.2 Radio properties

The most notable feature of the bright compact radio source associated with the BCG is a very steep lower-frequency component ( $\alpha \sim -2.0$ ) that dominates below 300 MHz, and whose spectral slope is comparable to that of the massive lobed source in MS 0735+74 ( $z = 0.21$ ; Cohen et al. 2005); it also shares with MS 0735+75 a similar rest-frame radio power of  $1.3 \times 10^{25} \text{ W Hz}^{-1}$ . The radio emission above 1 GHz has a significantly flatter spectrum ( $\alpha \sim -0.5$ ), comparable to that of the compact-core emission found in all line-emitting BCGs (Hogan et al. 2015) (but notably missing in MS 0735+74). In terms of radio power ( $7.3 \times 10^{24} \text{ W Hz}^{-1}$  at 10 GHz), the core emission of the BCG in eMACS J0252 falls into the top 10 percentile of the distribution compiled by Hogan et al. (2015) while the more extended, steep-spectrum emission still ranks in the top third. These properties suggest that accretion onto the active nucleus on the BCG is ongoing at present, after a sustained period of activity in the past that powered the aged, steep-spectrum lobes. A low-frequency observation at higher resolution of this source would help constrain the timing and energetics of this past outburst.

Potential	$\Delta\alpha$ [arcsec]	$\Delta\delta$ [arcsec]	$e$	$\theta$ [deg]	$r_{\text{core}}$ [kpc]	$r_{\text{cut}}$ [kpc]	$\sigma$ [km s <sup>-1</sup> ]
Cluster	$3.0^{+0.5}_{-0.3}$	$-3.8^{+0.3}_{-0.6}$	$0.79^{+0.02}_{-0.02}$	$130.4^{+0.3}_{-1.4}$	$79^{+15}_{-4}$	[1000]	$1050^{+20}_{-18}$
BCG	[0.0]	[0.0]	$0.36^{+0.06}_{-0.37}$	$165^{+11}_{-14}$	[0]	$126^{+153}_{-8}$	$360^{+122}_{-19}$
$L^*$ galaxy	...	...	...	...	[0.15]	[45]	[158]

**Table 2.** Best-fit model parameters for the mass distribution of eMACS J0252. From left to right: mass component, position relative to the BCG ( $\Delta\alpha$  and  $\Delta\delta$ ), dPIE shape (ellipticity and orientation,  $e$  and  $\theta$ ), core and cut radii ( $r_{\text{core}}$  and  $r_{\text{cut}}$ ), and velocity dispersion ( $\sigma$ ). The final row lists the global parameters adopted for a galaxy at the characteristic luminosity  $L^*$ , which is scaled to match the observed luminosity each of cluster member. Values in square brackets denote *a priori* settings that are kept fixed during the optimization setting.

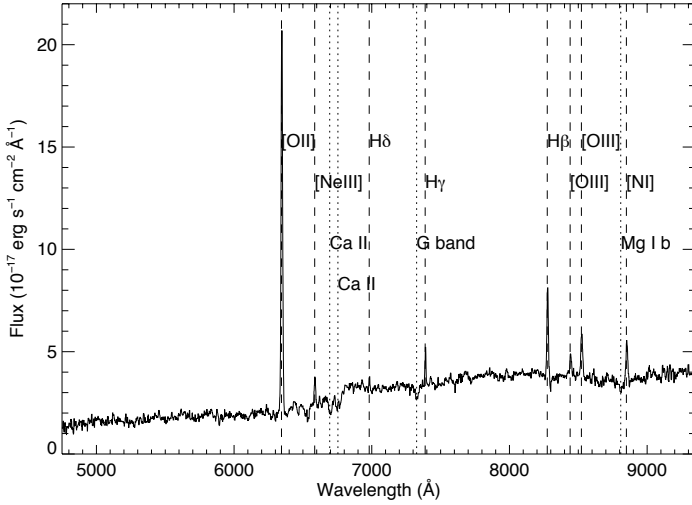


**Figure 5.** Spectrum of the BCG of eMACS J0252, as recorded by MUSE and corrected for Galactic extinction using  $E(B - V) = 0.028$  as measured by Schlafly & Finkbeiner (2011); notable emission and absorption features are labeled and marked by dashed and dotted lines, respectively. The extraction region of this spectrum is outlined in Fig. 6.

### 3.2.3 Stellar populations and star formation

Strong absorption features, such as Ca II (H+K), the G band, and Mg I b, in the spectrum of the BCG, as well as a pronounced Balmer break in the continuum, unequivocally establish the presence of an old stellar population, as found in all elliptical galaxies (Fig. 5). Rare in average ellipticals (but not uncommon in BCGs; Green et al. 2016, and references therein) is the pronounced line emission seen in Fig. 5.

From the [O II]  $\lambda 3727\text{\AA}$  emission-line flux recorded in our MUSE observation we measure a high star-formation rate of  $85 M_{\odot} \text{ yr}^{-1}$ , following Kennicutt (1989). Although this value accounts for both Galactic extinction and intrinsic extinction as estimated from the observed Balmer decrement, the latter is flux-weighted and thus biased against high-extinction regions. Indeed the corresponding  $E(B - V)$  value of about 0.05 appears unphysically low for the derived high intrinsic [O II]  $\lambda 3727\text{\AA}$  emission-line luminosity of  $6.1 \times 10^{42} \text{ erg s}^{-1}$ , a combination that is in stark conflict with the correlation found by Kewley et al. (2004). Considering, in addition, the compelling evidence of a dust lane (apparent in the short *HST* SNAPshot shown in Fig. 1), we therefore consider the quoted intrinsic extinction and the corresponding star-formation rate lower limits. The lack of a detection in the SCUBA2 observations, however, places a corresponding  $3\text{-}\sigma$  upper limit of  $300 M_{\odot} \text{ yr}^{-1}$  on the BCG star-formation rate. Both limits are shown in Fig. 8 and identify the BCG of eMACS J0252 as an extreme system in terms of star-formation rate.

We note that a contribution to the observed [O II] flux from nuclear activity can not be ruled out. Not only do the system’s radio properties suggest the presence of an AGN, the ratio of the fluxes of the [O III] and H $\beta$  emission lines of  $\log([O III]/H\beta) = -0.25$  also places the BCG of eMACS J0252 in the composite region of the BPT diagram (Baldwin et al. 1981). A correction for any AGN contribution to the [O II] flux (and hence the deduced star-formation rate) will require near-infrared spectroscopy to determine the H $\alpha$  emission-line flux.

### 3.2.4 Galaxy dynamics

Using the pPXF code of Cappellari & Emsellem (2004), we measure the central stellar velocity dispersion of the BCG to be  $(380 \pm 30) \text{ km s}^{-1}$ , well above the average value of  $260 \text{ km/s}$  for BCGs in the local Universe (Lauer et al. 2014) and high for BCGs at any redshift (Sohn et al. 2020).

The strong [O II] emission from the BCG (Fig. 5) extends to over 20 kpc in radius from the galactic centre, as shown in Fig. 6. In order to constrain the BCG’s kinematics, we track the spectral location and shape of the [O II] line across the full extent of this region. We interpret the recorded shifts of the centroid of the [O II] line as being caused by changes in the radial component of the peculiar velocity of the ISM, noting that variations in the ratio of the strengths of the  $3726.0\text{\AA}$  and  $3728.7\text{\AA}$  lines that make up the [O II] doublet<sup>3</sup> can not account for the observed spectral shifts. The resulting map of the BCG’s radial-velocity field is shown in Fig. 7. Unlike some line-emitting BCGs at lower redshift (Hamer et al. 2016), the BCG of eMACS J0252 shows no pronounced velocity asymmetry indicative of rotation or bulk motions associated with “sloshing” (first described by Markevitch et al. 2000), but instead a radial gradient of  $(90 \pm 30) \text{ km s}^{-1}$  amplitude that is consistent with radial infall of gas: the highest (positive) radial velocities are observed near the galactic centre, and no motion is detected at the largest radii (in projection) where infall is perpendicular to our line of sight. The timescale for infall from 30 kpc at this velocity is 330 Myr, in good qualitative agreement with the cooling times of about 1 Gyr observed for fully relaxed cool-core clusters (e.g., Hudson et al. 2010).

The above interpretation of the radial-velocity pattern shown in Fig. 7 as being indicative of isotropic infall requires the gas within the shown region to be optically thick<sup>4</sup>. Although speculative for eMACS J0252 at this point, this assumption is consistent with the high reddening values of  $E(B - V) \approx 0.6$  measured in the centres

<sup>3</sup> Such variations would be indicative of changes in the electron density (Osterbrock 1974).

<sup>4</sup> If the gas around the BCG were optically thin, like the ICM over most of the cluster volume, [O II] emission would be detectable both from gas in front and behind the BCG; as a result, isotropic infall would create no net shift of the [O II] line but only an effective broadening.



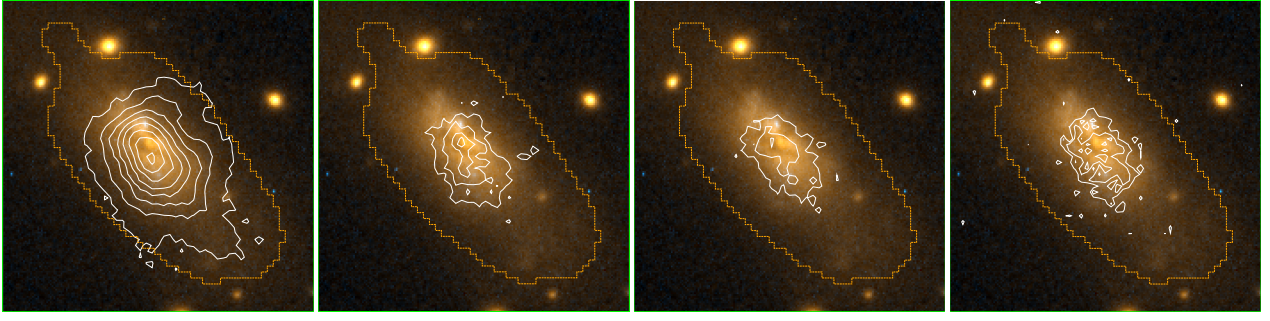


**Figure 6.** Contours (linearly spaced) of the emission-line flux from the BCG of eMACS J0252 as observed with MUSE, overlaid on the *HST* image shown in Fig. 1; the shown region spans  $10.5''$  on a side (75 kpc at the cluster redshift). Left to right: [O II], H $\beta$ , [O III], and [Ne III]. The region from which the BCG spectrum shown in Fig. 5 was extracted is delineated by the dashed orange line.

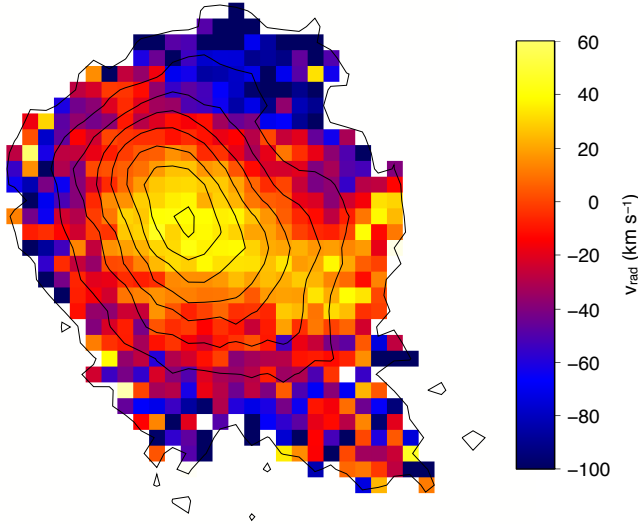


**Figure 7.** Radial velocity distribution derived from the observed wavelength of the [O II] line, as recorded by MUSE. The overlaid contours show the [O II] line flux for reference and scale (see also Fig. 6).

of massive cool-core clusters (O’Dea et al. 2010; McDonald et al. 2013) and excess absorption equivalent to neutral-hydrogen column densities of several  $10^{21} \text{ cm}^{-2}$  (e.g., McDonald et al. 2019).

#### 4 DISCUSSION AND CONCLUSIONS

As galaxy clusters grow through mergers and accretion, so do the giant ellipticals in their cores. The physical processes involved are closely intertwined, and the timescales involved are huge: it takes Gyrs for a cluster to dynamically relax after a merger, and it takes Gyrs for extremely luminous and extended cD galaxies to form in their centers. As a result, discoveries of highly evolved systems at high redshift offer rare opportunities to constrain the timeline of structure formation and growth at large look-back times.

The discovery of eMACS J0252 represents such an opportunity. At the system’s redshift of  $z = 0.703$ , the Universe is only a little over half its present age old, and yet the BCG of eMACS J0252 appears to have already evolved into one of the most massive galaxies known at *any* epoch. Specifically, eMACS J0252 and its BCG meet all of the following criteria for highly evolved, massive systems:

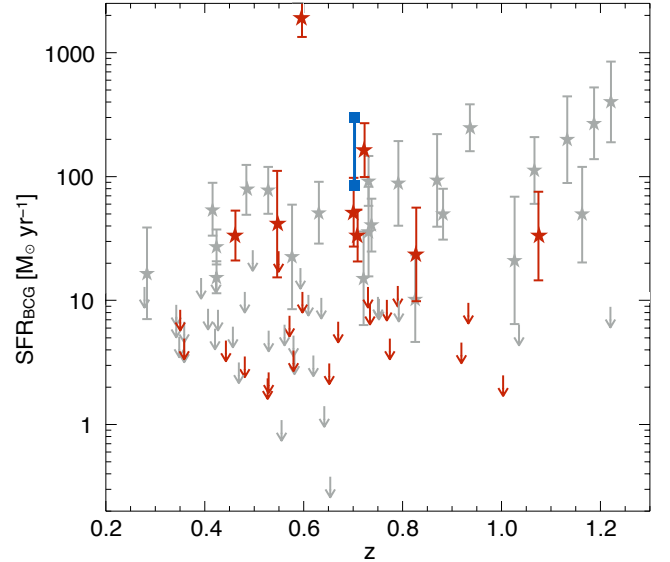


**Figure 8.** Locus of the BCG of eMACS J0252 in the SFR vs redshift plane for BCGs (adapted from McDonald et al. 2016). Grey and red symbols represent BCGs in disturbed and relaxed clusters, respectively. Our data point, added in blue, is shown as a range from the lower to the upper limit, set by our MUSE and SCUBA2 observations, respectively.

- Presence of a single, extremely luminous BCG;
- Excellent alignment between the major axes of the BCG and the overall galaxy distribution;
- High cluster velocity dispersion (over  $1,000 \text{ km s}^{-1}$ ), high X-ray luminosity (over  $1 \times 10^{45} \text{ erg s}^{-1}$ ), and high central mass ( $M(r < 250 \text{ kpc}) \sim 2 \times 10^{14} M_{\odot}$ );
- No evidence of substructure along the line of sight;
- A prodigiously star forming BCG that, at comparable redshifts, is only surpassed by the Phoenix Cluster ( $z = 0.597$ );
- Evidence of a radial flow of gas within 10 to 20 kpc of the BCG, traced by variations in the observed wavelength of the [O II] line;
- Presence of radio emission suggestive of sustained nuclear activity characteristic of AGN feedback in cool-core clusters.

Of the characteristics listed above, one in particular stands out: the detection of a radial flow of star-forming gas in the immediate vicinity of the BCG. Although the observed velocity pattern is fully consistent with isotropic infall, this interpretation holds only if the gas in the immediate vicinity ( $r \leq 20 \text{ kpc}$ ) is optically thick, a speculative assumption that is at present only supported by the potentially

high density of the ICM in the very centre of cool cluster cores and the presence of visible dust lanes across the BCG of eMACSJ0252. If confirmed as an isotropic flow by in-depth follow-up studies, the signature of radial infall seen in Fig. 7 (expected from, and fully consistent with, extensive studies of feedback processes in the cores of relaxed clusters (for a recent review see, e.g., [McNamara & Nulsen 2012](#))) would constitute, to the best of our knowledge, the first direct kinematic confirmation of the cooling-flow picture advanced by [Fabian et al. \(1984\)](#).

In addition, the extreme ellipticity of both the BCG and the cluster-scale dark-matter distribution of its host cluster (as constrained by our strong-lensing mass model) deserves special emphasis. At  $e = 0.8$ , the ellipticity of eMACSJ0252 provides a rare glimpse of the extreme end of the cluster-halo shape distribution for comparison with predictions from numerical simulations ([Harvey et al. 2020](#)).

Although the existing observational data have established eMACSJ0252 unambiguously as an exceptional cluster, dominated by an equally exceptional BCG, our knowledge of the system remains preliminary in several important areas. Specifically the measurement of key characteristics of the BCG (AGN properties, gas and dust content, morphology, size of core / nuclei, full extent and profile of diffuse halo, etc) is hampered by the limited depth and spectral coverage of the existing data. Even more important, however, will be a robust determination of the fundamental properties and dynamic state of the BCG's cluster environment characterized, for instance, by the presence of a prominent cool core, a task that will require dedicated follow-up observations across the electromagnetic spectrum, in particular high-resolution X-ray imaging spectroscopy of the intracluster medium.

## ACKNOWLEDGEMENTS

IRS and ACE acknowledge support from STFC (ST/T000244/1). Based on observations obtained at the international Gemini Observatory, a program of NSF's NOIRLab, which is managed by the Association of Universities for Research in Astronomy (AURA) under a cooperative agreement with the National Science Foundation on behalf of the Gemini Observatory partnership: the National Science Foundation (United States), National Research Council (Canada), Agencia Nacional de Investigación y Desarrollo (Chile), Ministerio de Ciencia, Tecnología e Innovación (Argentina), Ministério da Ciência, Tecnologia, Inovações e Comunicações (Brazil), and Korea Astronomy and Space Science Institute (Republic of Korea). Also based on observations made with the NASA/ESA *Hubble Space Telescope*, obtained from the Data Archive at the Space Telescope Science Institute, which is operated by the Association of Universities for Research in Astronomy, Inc., under NASA contract NAS 5-26555. These observations are associated with program GO-15307. Some of the data presented herein were obtained at the W.M. Keck Observatory, which is operated as a scientific partnership among the California Institute of Technology, the University of California, and the National Aeronautics and Space Administration. The Observatory was made possible by the generous financial support of the W.M. Keck Foundation. The authors wish to recognize and acknowledge the very significant cultural role and reverence that the summit of Maunakea has always had within the indigenous Hawaiian community. We are most fortunate to have the opportunity to conduct observations from this mountain.

## DATA AVAILABILITY

The data underlying this article are available in the MAST, VLT, and Keck data archives.

## REFERENCES

- Albert C. E., White R. A., Morgan W. W., 1977, *ApJ*, **211**, 309  
 Baldwin J. A., Phillips M. M., Terlevich R., 1981, *PASP*, **93**, 5  
 Beers T. C., Geller M. J., 1983, *ApJ*, **274**, 491  
 Bellstedt S., et al., 2016, *MNRAS*, **460**, 2862  
 Bleem L. E., et al., 2020, *ApJS*, **247**, 25  
 Bonaventura N. R., et al., 2017, *MNRAS*, **469**, 1259  
 Cappellari M., Emsellem E., 2004, *PASP*, **116**, 138  
 Cohen A. S., Clarke T. E., Feretti L., Kassim N. E., 2005, *ApJ*, **620**, L5  
 Coziol R., Andernach H., Caretta C. A., Alamo-Martínez K. A., Tago E., 2009, *AJ*, **137**, 4795  
 De Lucia G., Blaizot J., 2007, *MNRAS*, **375**, 2  
 Donahue M., et al., 2015, *ApJ*, **805**, 177  
 Donzelli C. J., Muriel H., Madrid J. P., 2011, *ApJS*, **195**, 15  
 Dressler A., 1984, *ARA&A*, **22**, 185  
 Ebeling H., et al., 2013, *MNRAS*, **432**, 62  
 Faber S. M., et al., 2003, in Iye M., Moorwood A. F. M., eds, Society of Photo-Optical Instrumentation Engineers (SPIE) Conference Series Vol. 4841, Instrument Design and Performance for Optical/Infrared Ground-based Telescopes. pp 1657–1669, doi:10.1117/12.460346  
 Fabian A. C., Nulsen P. E. J., Canizares C. R., 1984, *Nature*, **310**, 733  
 Gladders M. D., et al., 2019, Building the SPT-HST Legacy: Imaging Massive Clusters to  $z=1.5$ , HST Proposal  
 Green T. S., et al., 2016, *MNRAS*, **461**, 560  
 Hamer S. L., et al., 2016, *MNRAS*, **460**, 1758  
 Harvey D., Robertson A., Tam S.-I., Jauzac M., Massey R., Rhodes J., McCarthy I. G., 2020, *MNRAS*,  
 Herbonnet R., von der Linden A., Allen S. W., Mantz A. B., Modumudi P., Morris R. G., Kelly P. L., 2019, *MNRAS*, **490**, 4889  
 Hogan M. T., et al., 2015, *MNRAS*, **453**, 1201  
 Hudson D. S., Mittal R., Reiprich T. H., Nulsen P. E. J., Andernach H., Sarazin C. L., 2010, *A&A*, **513**, A37  
 Jauzac M., et al., 2015, *MNRAS*, **452**, 1437  
 Jullo E., Kneib J. P., Limousin M., Elíasdóttir Á., Marshall P. J., Verdugo T., 2007, *New Journal of Physics*, **9**, 447  
 Kennicutt Robert C. J., 1989, *ApJ*, **344**, 685  
 Kewley L. J., Geller M. J., Jansen R. A., 2004, *AJ*, **127**, 2002  
 Kluge M., et al., 2020, *ApJS*, **247**, 43  
 Koekemoer A. M., et al., 2011, *ApJS*, **197**, 36  
 Kormendy J., Djorgovski S., 1989, *ARA&A*, **27**, 235  
 Lauer T. R., Postman M., Strauss M. A., Graves G. J., Chisari N. E., 2014, *ApJ*, **797**, 82  
 Limousin M., et al., 2016, *A&A*, **588**, A99  
 Lin Y.-T., Mohr J. J., 2004, *ApJ*, **617**, 879  
 Mann A. W., Ebeling H., 2012, *MNRAS*, **420**, 2120  
 Markevitch M., et al., 2000, *ApJ*, **541**, 542  
 Masters D., Capak P., 2011, *PASP*, **123**, 638  
 Matthews T. A., Morgan W. W., Schmidt M., 1964, *ApJ*, **140**, 35  
 McDonald M., et al., 2012, *Nature*, **488**, 349  
 McDonald M., Benson B., Veilleux S., Bautz M. W., Reichardt C. L., 2013, *ApJ*, **765**, L37  
 McDonald M., et al., 2014, *ApJ*, **784**, 18  
 McDonald M., et al., 2016, *ApJ*, **817**, 86  
 McDonald M., et al., 2019, *ApJ*, **885**, 63  
 McNamara B. R., Nulsen P. E. J., 2012, *New Journal of Physics*, **14**, 055023  
 McNamara B. R., O'Connell R. W., 1989, *AJ*, **98**, 2018  
 McNamara B. R., et al., 2006, *ApJ*, **648**, 164  
 Merritt D., 1984, *ApJ*, **276**, 26  
 Newman A. B., Treu T., Ellis R. S., Sand D. J., 2013, *ApJ*, **765**, 25  
 Nurgaliev D., et al., 2017, *ApJ*, **841**, 5  
 O'Dea C. P., et al., 2008, *ApJ*, **681**, 1035



- O'Dea K. P., et al., 2010, *ApJ*, **719**, 1619  
 Oemler A. J., 1976, *ApJ*, **209**, 693  
 Osterbrock D. E., 1974, *Astrophysics of gaseous nebulae*  
 Piqueras L., Conseil S., Shepherd M., Bacon R., Leclercq F., Richard J., 2019, in Molinaro M., Shorridge K., Pasian F., eds, *Astronomical Society of the Pacific Conference Series Vol. 521, Astronomical Data Analysis Software and Systems XXVI*. p. 545  
 Planck Collaboration et al., 2016, *A&A*, **594**, A27  
 Richard J., et al., 2020, arXiv e-prints, p. arXiv:2009.09784  
 Schlafly E. F., Finkbeiner D. P., 2011, *ApJ*, **737**, 103  
 Schneider D. P., Gunn J. E., Hoessel J. G., 1983, *ApJ*, **268**, 476  
 Schombert J. M., 1986, *ApJS*, **60**, 603  
 Shin T.-h., Clampitt J., Jain B., Bernstein G., Neil A., Rozo E., Rykoff E., 2018, *MNRAS*, **475**, 2421  
 Sohn J., Geller M. J., Diaferio A., Rines K. J., 2020, *ApJ*, **891**, 129  
 Thuan T. X., Romanishin W., 1981, *ApJ*, **248**, 439  
 Tonry J. L., 1985, *AJ*, **90**, 2431  
 Trudeau A., et al., 2019, *MNRAS*, **487**, 1210  
 Voges W., et al., 1999, *A&A*, **349**, 389  
 Weilbacher P. M., et al., 2020, *A&A*, **641**, A28  
 Wen Z. L., Han J. L., 2013, *MNRAS*, **436**, 275

This paper has been typeset from a  $\text{\LaTeX}$  file prepared by the author.

## APPENDIX A: SPECTROSCOPIC REDSHIFTS

We list in Table A1 all galaxies for which spectroscopic redshifts were measured by us with the MUSE and DEIMOS spectrographs (see Section 2.3 for details).

R.A. (J2000) Dec.	$z$	R.A. (J2000) Dec	$z$
02 52 13.86 −20 58 56.6	0.7381	02 52 27.03 −21 00 56.2	0.7031
02 52 14.05 −20 58 06.6	0.4874	02 52 27.06 −21 00 52.9	0.7029
02 52 14.75 −20 59 19.6	0.6623	02 52 27.17 −21 00 57.0	0.7083
02 52 15.20 −20 59 43.1	0.5856	02 52 27.22 −21 00 52.0	0.7022
02 52 15.25 −21 00 20.9	0.4876	02 52 27.32 −21 00 43.9	0.7056
02 52 15.69 −20 58 42.8	0.7636	02 52 27.32 −21 00 43.9	0.7056
02 52 16.63 −21 03 05.3	0.7038	02 52 27.34 −21 00 47.8	0.7141
02 52 19.22 −21 01 59.8	0.6738	02 52 27.51 −21 00 49.0	0.7026
02 52 20.20 −21 01 48.4	0.7033	02 52 27.56 −21 01 15.4	1.0175
02 52 20.53 −21 01 43.3	0.7007	02 52 27.65 −21 00 39.7	0.7011
02 52 21.31 −21 02 08.3	0.6706	02 52 27.70 −21 00 48.4	0.7009
02 52 22.11 −21 01 06.2	0.4929	02 52 27.70 −21 00 29.8	0.5974
02 52 22.71 −21 01 55.8	0.6712	02 52 27.71 −21 01 15.2	0.9333
02 52 23.26 −21 00 20.0	0.7100	02 52 27.79 −21 00 21.1	1.0190
02 52 23.36 −21 01 43.2	0.6792	02 52 28.00 −21 00 28.3	0.5907
02 52 24.94 −21 00 46.2	0.6990	02 52 28.16 −21 00 31.6	0.7009
02 52 25.30 −21 01 03.6	1.0200	02 52 28.23 −21 00 52.4	0.5970
02 52 25.31 −21 00 14.0	0.7051	02 52 28.28 −21 00 51.2	0.7073
02 52 25.38 −21 01 07.9	1.1284	02 52 28.35 −21 00 25.4	0.7095
02 52 25.48 −21 00 52.4	1.0162	02 52 28.37 −21 00 40.8	0.6925
02 52 25.51 −21 01 00.0	1.0169	02 52 28.44 −21 01 07.4	0.7002
02 52 25.86 −21 00 43.0	0.7012	02 52 29.03 −20 59 26.5	0.6968
02 52 25.95 −21 00 23.8	0.0000	02 52 29.05 −21 00 39.4	0.7025
02 52 26.05 −21 01 17.5	0.4918	02 52 29.17 −21 00 38.3	0.7024
02 52 26.08 −21 00 50.4	1.0154	02 52 29.21 −21 00 26.5	0.7010
02 52 26.10 −21 01 10.5	1.1288	02 52 29.40 −21 01 12.3	0.4855
02 52 26.23 −21 00 55.7	0.6988	02 52 29.52 −21 01 16.6	1.1349
02 52 26.24 −21 00 57.8	0.6989	02 52 29.54 −20 57 57.3	0.6963
02 52 26.29 −21 00 24.9	1.0143	02 52 29.60 −21 01 17.5	1.1348
02 52 26.46 −21 01 16.9	0.7124	02 52 29.69 −21 00 48.9	0.7041
02 52 26.47 −21 01 02.6	0.7007	02 52 30.29 −21 00 24.2	0.6954
02 52 26.59 −21 00 45.9	0.7022	02 52 30.34 −21 01 42.9	0.7077
02 52 26.60 −21 00 47.5	0.6966	02 52 30.40 −21 00 47.7	0.4886
02 52 26.61 −21 00 58.1	0.7031	02 52 30.75 −21 02 45.1	0.7082
02 52 26.62 −21 00 42.3	0.4623	02 52 31.21 −21 01 26.6	0.7063
02 52 26.65 −21 00 22.5	0.4364	02 52 31.43 −21 00 43.5	0.7058
02 52 26.66 −21 01 04.3	0.5975	02 52 32.69 −21 00 07.5	0.7015
02 52 26.67 −21 01 21.0	0.4927	02 52 33.53 −21 03 05.9	0.5914
02 52 26.71 −21 00 52.6	0.6882	02 52 35.14 −21 00 30.9	0.6926
02 52 26.74 −21 00 58.6	0.7126	02 52 35.32 −21 01 33.2	0.7036
02 52 26.78 −21 00 36.3	0.7062	02 52 36.76 −20 58 16.9	0.7011
02 52 26.84 −21 01 12.7	0.7106	02 52 38.68 −20 59 11.6	0.6910
02 52 26.91 −21 00 32.6	1.4546	02 52 38.94 −20 58 09.6	0.2889
02 52 26.94 −21 00 49.6	0.7037		

**Table A1.** Equatorial coordinates and spectroscopic redshifts of galaxies in the field of eMACSJ0252 as determined by us from MUSE and DEIMOS observations.